Int. J. Electrochem. Sci., 14 **(2019)** 9741 – 9754, doi: 10.20964/2019.10.26

International Journal of
ELECTROCHEMICAL
SCIENCE
www.electrochemsci.org

Experimental research on the counter-rotating electrochemical machining of 304 stainless steel and Inconel 718 alloy

Dengyong Wang[1,2,*], *Juchen Zhang*[3,1]

[1] College of Mechanical and Electrical Engineering, Nanjing University of Aeronautics and Astronautics, Nanjing, China
[2] Jiangsu Key Laboratory of Precision and Micro-Manufacturing Technology, Nanjing, China
[3] School of Mechanical Engineering, Hefei University of Technology, Hefei, China
*E-mail: wdy15150565695@163.com

Received: 5 June 2019 / *Accepted:* 23 July 2019 / *Published:* 30 August 2019

In Electrochemical machining (ECM), anodic dissolution process is strongly affected by the electrochemical behavior of the target metal. This study aims to improve the counter-rotating electrochemical machining (CRECM) performance of lug boss on Inconel 718 on basis of different dissolution behaviors of metals. The dissolved surfaces of 304 stainless steel and Inconel 718 at various current densities were examined using scanning electron microscope, energy-dispersive X-ray spectroscopy, and electrochemical impedance spectroscopy. The profiles and surface qualities of the machined lug bosses were compared. The results indicated that the 304 stainless steel workpiece presented substantially better machining performance than Inconel 718 due to its favorable localization effect. Straight lug bosses with small fillet radii were fabricated in 304 stainless steel. In contrast, the sidewall of a lug boss formed on the surface of Inconel 718 workpiece was tapered and had a large fillet radius because of substantial corrosion on its top surface. On this basis, a 304 stainless steel coating layer was employed to improve CRECM performance during machining of a high lug boss on Inconel 718. The experimental results showed that the employment of 304 stainless steel coating layer could prevent the surface of lug boss on Inconel 718 from dissolution and therefore improve the machining accuracy effectively.

Keywords: Electrochemical machining; Dissolution behavior; Machining performance; Lug boss; Coating layer

1. INTRODUCTION

Electrochemical machining (ECM) is a non-contact machining process that has become an important manufacturing technology in the aerospace industry. Unlike conventional mechanical methods, it can efficiently dissolve difficult-to-cut materials regardless of hardness, without tool wear or machining stress [1–3]. Some critical aero-engine components such as the blisk, diffuser, and casing parts have been fabricated by using ECM methods [4–6].

However, since the ECM process is based on anodic dissolution of the materials, the machining performance is affected substantially by the electrochemical dissolution behaviors of metals. Many studies have been performed concerning the anodic metal dissolution process. The ECM process of mild steel was studied in $NaNO_3$ solution, and anodic dissolution efficiencies were measured at various current densities [7–8]. The surfaces of 100Cr6 alloy corroded in $NaNO_3$ and NaCl solutions were compared and the microstructures of the surface films were analyzed [9]. The micro electrochemical surface and machining products from ECM of iron in $NaNO_3$ solution were investigated [10–12]. The anodic process and surface texture development of cobalt were studied [13]. The electrochemical dissolution behaviors of Ti90Al6V4 and Ti60Al40 titanium alloys were investigated in an electrolyte with chloride ions [14]. In addition, the dissolution of titanium alloy Ti6Al4V was studied under the ECM conditions and the surface roughness with different machining parameters was analyzed [15].

The studies reveal that different metal components lead to distinctly different anodic dissolution behaviors, as well as affecting ECM accuracy and surface quality. Here, the machining performances of 304 stainless steel and Inconel 718 alloy during counter-rotating electrochemical machining (CRECM) are focused on. CRECM is a newly proposed ECM method that is used to gain lug bosses on the surfaces of revolving workpieces such as aero-engine casings [16–18]. In CRECM, a revolving cathode tool with concave cavities is typically used. The cathode tool rotates synchronously with the anode workpiece in the opposite direction. Due to the unique shapes and movements of the electrodes, the anode shaping process in CRECM is quite different from that in conventional sinking ECM. In previous study, the anodic dissolution behaviors of stainless steel 304 and Inconel 718 were studied only at low current densities using plane electrodes [19]. The CRECM performances of these two types of metal have not been fully compared.

In this paper, the effects of the dissolution behaviors of 304 stainless steel and Inconel 718 on the formation of lug bosses are investigated experimentally, using the CRECM method. The microstructures of corroded surfaces at different current densities are examined using scanning electron microscope (SEM), energy-dispersive X-ray spectroscopy (EDX), and electrochemical impedance spectroscopy (EIS). The profiles and surface qualities of the machined lug bosses are analyzed. The results show that 304 stainless steel presents substantially better machining performance than Inconel 718 because of its favorable localization effect of anodic dissolution. On this basis, a 304 stainless steel coating layer is used to improve machining accuracy of a high lug boss on Inconel 718 during CRECM. The experimental results indicate that a 304 stainless steel coating layer can well protect the surface of the lug boss and remarkably improve the machining accuracy.

2. EXPERIMENTAL

2.1. Sample preparation

304 stainless steel and Inconel 718 samples with dimensions of 5 mm × 5 mm × 10 mm were prepared for the anodic dissolution tests. Inconel 718 and 304 stainless steel are two typical nickel-

chrome-iron alloys. The main components of 304 stainless steel are Fe (69.6%), Ni (8.9%), Cr (18.38%), Mn (2%), Si (1%), and some other impurities. The main components of Inconel 718 are Fe (18.9%), Ni (53.7%), Cr (18.2%), Nb (5.1%), Ti (1.1%), etc. The electrolyte was a 20% $NaNO_3$ solution at a temperature of 25 °C. The sample surfaces were polished carefully and then corroded at different current densities using a constant current power supply. The corrosion time in each experiment was controlled to be 30 s.

2.2. Microstructures after corrosion at various current densities

Fig. 1 shows the microstructures of 304 stainless steel samples corroded at current densities of 1 A/cm^2, 3 A/cm^2, 5 A/cm^2, 10 A/cm^2, and 50 A/cm^2. At a low current density of 1 A/cm^2, the surface is smooth without any evidence of corrosion. As the current density increases, corroded areas are observed on the surfaces at 3 A/cm^2, 5 A/cm^2, and 10 A/cm^2. When the current density reaches a high value of 50 A/cm^2, a smooth surface with traces of corrosion is observed, which indicates that the materials on the surface are dissolved uniformly.

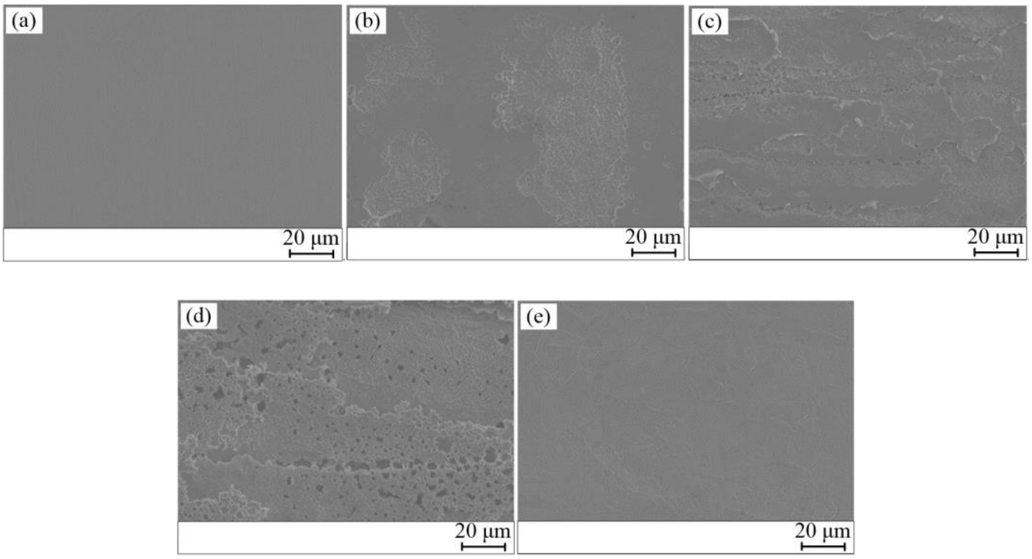

Figure 1. Microstructures of 304 stainless steel samples corroded at various current densities. (a) 1A/cm^2; (b) 3A/cm^2; (c) 5A/cm^2; (d) 10A/cm^2; (e) 50A/cm^2.

Fig. 2 shows the microstructures of corroded Inconel 718 surfaces. From the SEM image shown in Fig. 2 (a), serious pitting corrosion is observed on the surface at 1 A/cm^2. The elemental compositions of undissolved region A and corrosion pitted region B were analyzed using EDX (Fig. 3). The main components of the metal in region A match that of the base material. However, the carbon and oxygen concentrations are remarkably higher in region B, which indicates the formation of carbides and oxides within the corrosion pits. Compared with that of 304 stainless steel, the surface quality of Inconel 718 is substantially poorer at a low current density of 1 A/cm^2. The pitting corrosion can be eliminated gradually by increasing the current density. Only minor corrosion pits remain on the corroded surface at 3 A/cm^2 and smooth surfaces are obtained when the current density exceeds 5 A/cm^2.

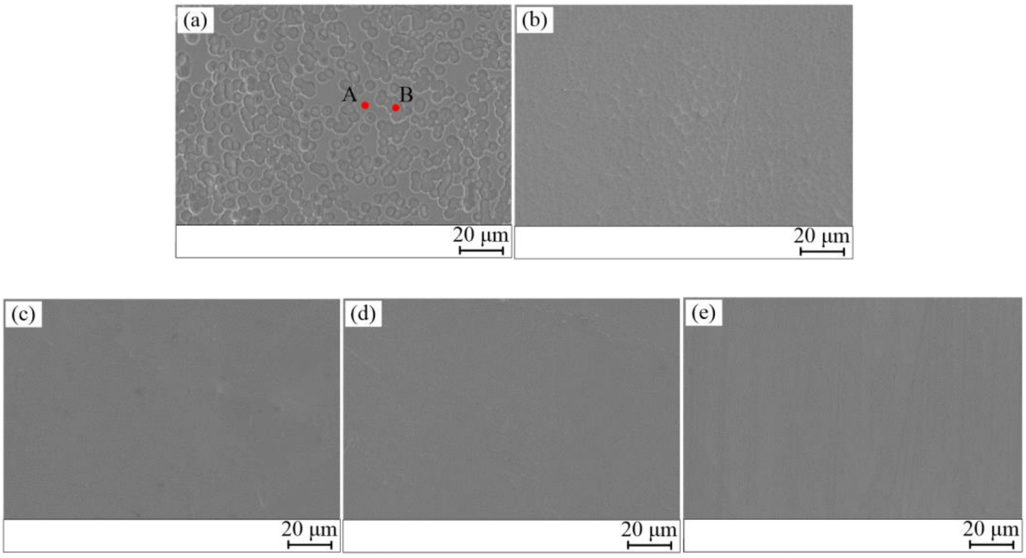

Figure 2. Microstructures of Inconel 718 samples corroded at various current densities. (a) 1A/cm^2; (b) 3A/cm^2; (c) 5A/cm^2; (d) 10A/cm^2; (e) 50A/cm^2.

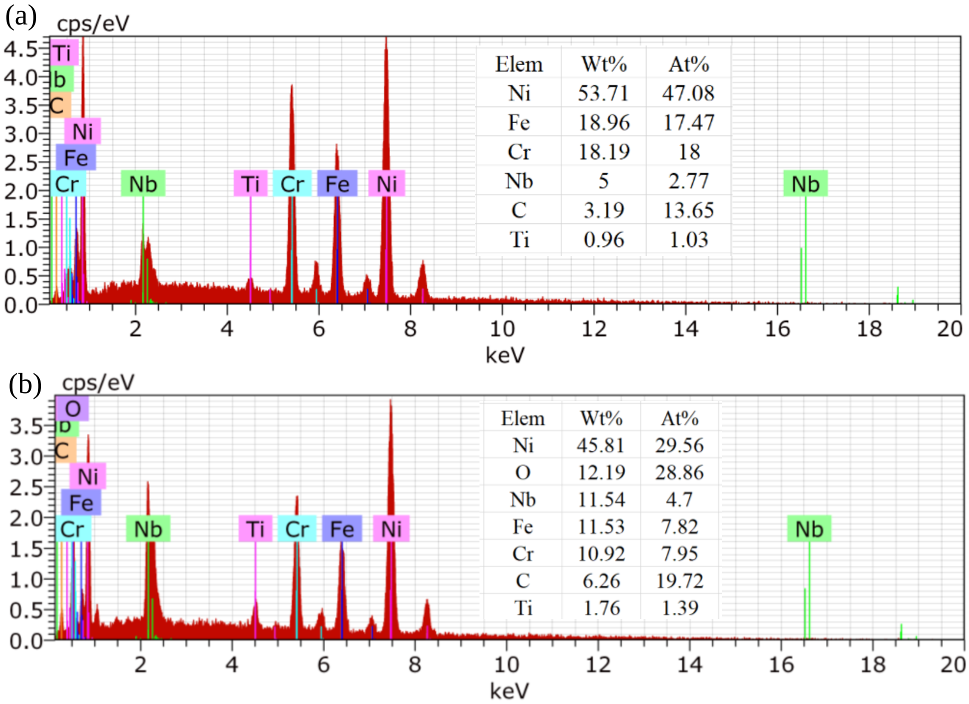

Elem	Wt%	At%
Ni	53.71	47.08
Fe	18.96	17.47
Cr	18.19	18
Nb	5	2.77
C	3.19	13.65
Ti	0.96	1.03

Elem	Wt%	At%
Ni	45.81	29.56
O	12.19	28.86
Nb	11.54	4.7
Fe	11.53	7.82
Cr	10.92	7.95
C	6.26	19.72
Ti	1.76	1.39

Figure 3. Elemental compositions of the (a) undissolved region and (b) corrosion pitted regions.

2.3. Electrochemical impedance spectroscopy

According to the SEM images shown in Figs. 1 (a) and 2 (a), the surface morphologies of 304 stainless steel and Inconel 718 are quite different. The surface of 304 stainless steel corroded at 1A/cm^2 is well preserved without any corrosion. However, the surface of Inconel 718 suffers serious pitting corrosion. In this section, the surfaces of the two kinds of material corroded at the low current density of 1 A/cm^2 were further examined by using EIS. Fig. 4 shows the Nyquist plots and corresponding fitted electrical equivalent circuits. The Nyquist plots in Fig. 4(a) indicate that the corrosion resistance of 304 stainless steel is higher than that of Inconel 718 [20–21]. Two different electrical equivalent circuits were obtained using Zview software. The fitted circuit for 304 stainless steel includes only one time constant. This time constant results from the presence of a compact passive film [22], as shown in Fig. 4(b). According to the simulated data in Table 1, the resistance of the passive film R_p is 2.05×10^7 Ω·cm^2. In contrast, the electrical equivalent circuit for Inconel 718 requires a second time constant due to the corrosion pits on the surface (Fig. 4(c)) [23]. The electrolyte resistance inside the corrosion pits (R_1) was calculated to be 58.89 Ω·cm^2 and the resistance of the passive film R_p is 4.83×10^6 Ω·cm^2, which is much smaller than that of 304 stainless steel. It can be deduced that a compact passive film is formed on the surface of 304 stainless steel at low current densities and as a result the surface are protected from corrosion. In contrast, the passive film formed on the surface of Inconel 718 is defective, resulting in a serious pitting corrosion even at a low current density.

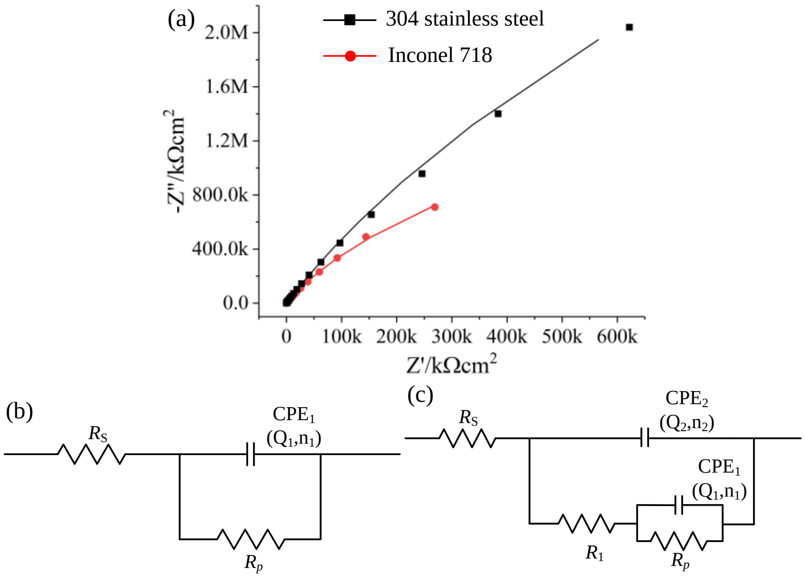

Figure 4. Nyquist plots and fitted electrical equivalent circuits for 304 stainless steel and Inconel 718. (a) Nyquist plots; (b) Electrical equivalent circuit for 304 stainless steel; (c) Electrical equivalent circuit for Inconel 718. R_s is the solution resistance, R_p is the resistance of passive film, the constant phase-angle element CPE$_1$ is the double layer capacitance, and CPE$_2$ is the oxide film capacitance. R_1 is the electrolyte resistance inside the corrosion pit.

Table 1. Data obtained from the equivalent circuits.

Metal	R_S/Ωcm^2	Q_1/μF cm^{-2}	n_1	R_p/Ωcm^2	Q_2/μF cm^{-2}	n_2	R_1/Ωcm^2
304 stainless steel	9.77	3.69x10^{-6}	0.89	2.05x10^7	-	-	-
Inconel 718	11.62	4.15x10^{-6}	0.88	4.83x10^6	5.38x10^{-6}	0.87	58.89

2.4. CRECM of lug bosses

Fig. 5 shows the experimental apparatus used in the CRECM process. The cylindrical anode workpiece and cathode tool were fixed on two synchronously counter-rotating spindles. A horizontal moving platform was used to realize the feed motion of the cathode tool. An electrolyte circulation system was developed to maintain rapid product renewal in the inter-electrode gap. To machine lug bosses on the surface of anode workpiece, a revolving cathode tool with certain number of concave cavities were designed particularly. When a constant potential difference was applied between the anode workpiece and cathode tool, the materials of the anode workpiece were dissolved gradually, and lug bosses were fabricated at the corresponding areas of the concave cavities. The cylindrical stainless steel 304 and Inconel 718 workpieces with a diameter of 50 mm were used. A stainless steel cylinder with five concave cavities was employed as the cathode tool, as shown in Fig. 6. The relevant experimental conditions are listed in Table 2.

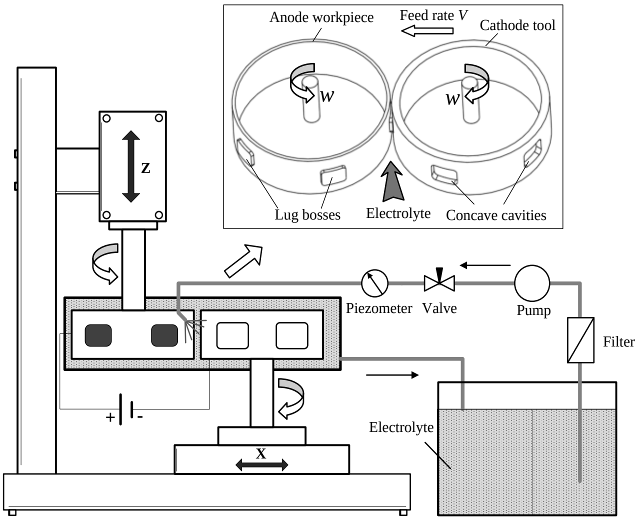

Figure 5. CRECM experimental apparatus.

Figure 6. Cylindrical cathode tool used in CRECM.

Table 2. Relevant experimental conditions in CRECM.

Parameter	Value
Materials of anode workpieces	304 stainless steel, Inconel 718
Diameter of anode workpiece	Φ50 mm
Material of cathode tool	Stainless steel 304
Diameter of cathode tool	Φ50 mm
Potential difference	8V
Electrolyte	20% $NaNO_3$
Initial inter-electrode gap	0.2mm
Spindle rotation speed	1 rpm
Feed rate of cathode tool	0.015 mm/min, 0.02 mm/min
Amount of cathode feed	2.5 mm

3. RESULTS AND DISCUSSION

3.1. Comparison of machining performance

As shown in Fig. 7, lug bosses were fabricated on the cylindrical surfaces of 304 stainless steel and Inconel 718 workpieces. A significant difference in the machining performances of the two metals is observed visually. From the front view shown in Fig. 7(a), the lug boss on 304 stainless steel is white with a smooth surface. However, the lug boss on Inconel 718 exhibits a rough surface (Fig. 7(b)). The surfaces of the lug bosses were examined using SEM. As shown in Fig. 8(a), the microstructure of 304 stainless steel indicates that the surface of the lug boss is absence of corrosion due to the formation of a compact passive film. In contrast, a serious corroded surface is visible for the lug boss on Inconel 718 (Fig. 8(b)).

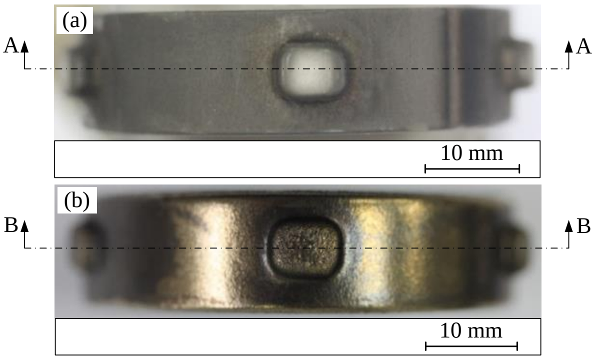

Figure 7. Front views of the machined workpieces. (a) 304 stainless steel; (b) Inconel 718.

The machined workpieces were divided along the cross-sections using wire cut electrical discharge machining, as shown in Fig. 9. The lug boss on 304 stainless steel shown in Fig. 9(a) exhibits straight sidewall profiles and small fillet radii, which indicates favorable machining performance. For Inconel 718, the machining accuracy of the lug boss is substantially poorer due to the tapered sidewalls and large fillet radii. Fig. 10 shows the contour lines of lug bosses measured using a coordinate measuring machine. The sidewall taper angle of lug boss on the 304 stainless steel is only 0.13 ° and the fillet radius is 0.75 mm. In contrast, the sidewall of the Inconel 718 structure exhibits a large taper angle of 19.2° with a fillet radius of 1.24 mm. The depth of corrosion on the top of the lug boss can be as high as 0.63 mm.

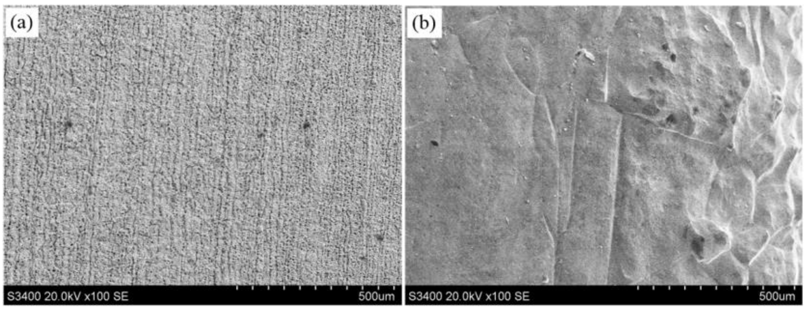

Figure 8. Microstructures of the surfaces of lug bosses. (a) 304 stainless steel; (b) Inconel 718.

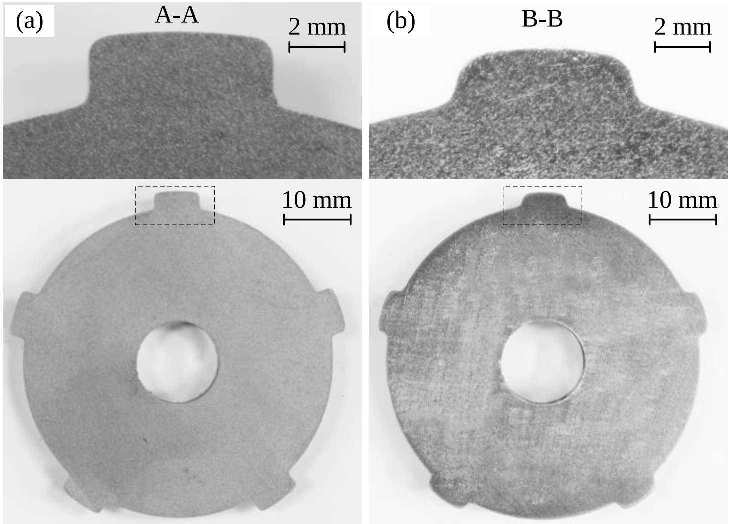

Figure 9. Cross-sections of the lug bosses. (a) 304 stainless steel; (b) Inconel 718.

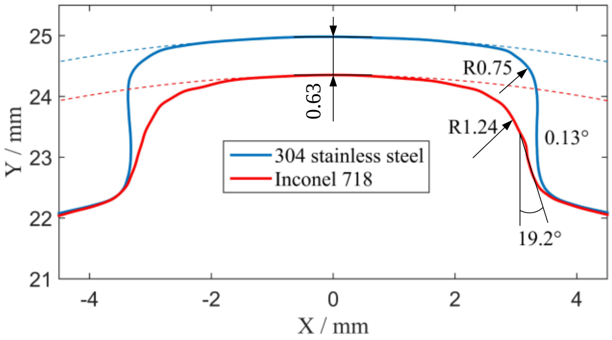

Figure 10. Comparison of the contour lines of lug bosses on 304 stainless steel and Inconel 718.

Fig. 11 shows the workpieces machined using only a single rotation of electrodes in CRECM. The total processing time is 1 min. A clear white pattern was printed on the 304 stainless steel surface. However, Inconel 718 surface was quickly corroded and the shape of the printed pattern was blurred.

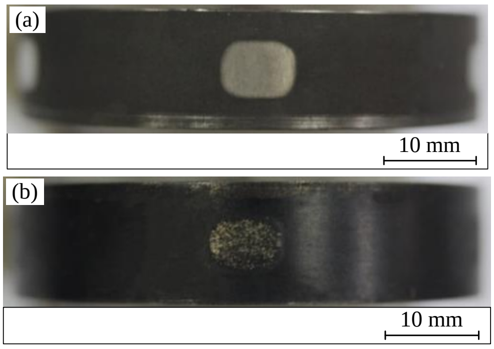

Figure 11. Workpieces using only a single rotation of electrodes in CRECM. (a) 304 stainless steel; (b) Inconel 718.

To illustrate the different machining performances of 304 stainless steel and Inconel 718, the electric field in CRECM was simulated. The potentials applied to the anode and workpiece were 8 V and 0 V, respectively. The potential distribution in the electrolyte domain satisfied the Laplace equation [24–26]:

$$\frac{\partial^2 \varphi}{\partial x^2} + \frac{\partial^2 \varphi}{\partial y^2} = 0 \tag{1}$$

The boundary conditions for the anode workpiece and cathode tool were:

$$\varphi \mid \Gamma_1 = 8 \quad \text{(along the anode workpiece)} \tag{2}$$

$$\varphi \mid \Gamma_2 = 0 \quad \text{(along the cathode tool)} \tag{3}$$

$$\frac{\partial \varphi}{\partial n} \mid \Gamma_3 = 0 \quad \text{(along the concave cavity)} \tag{4}$$

$$\frac{\partial \varphi}{\partial n} \mid \Gamma_{4-7} = 0 \quad \text{(along the additional surfaces)} \tag{5}$$

The finite element method on basis of COMSOL software was used to calculate the electric field distribution. Fig. 12 shows the current density distribution at a rotation angle of 0°. The area where the current density exceeds 1A/cm^2 is highlighted in red. The enlarge view shows that the current density at the margins of the surface of lug boss exceeds 1 A/cm^2. Even in the central area, the current density can reach approximately 0.6 A/cm^2. Stray current lines are observed travelling from the surface of lug boss to the edges of the concave cavity.

Fig. 13 shows the current density at the midpoint *P* of the surface of lug boss at rotation angles ranging from -180° to 180°. The maximum current density at point *P* is only 1.58 A/cm^2. It is well known that the use of passivating $NaNO_3$ solution can help localize the anodic dissolution of iron and iron-based alloys [27-28]. For 304 stainless steel, the current efficiency of anodic dissolution effciency in $NaNO_3$ solution is strongly dependent on the current density [29-30]. The current efficency is very small at low current density, and increases gradually with the current density. According to our previsous study [19], the current efficiency of 304 stainless steel tends to be near 0% at low current densities up to 2.45 A/cm^2, as shown in Fig. 14. The small current efficiency can be attribiuted to the formation of a compact passive film with a few to tens of nanometers thickness on the surface at low current density [31-32]. During the ECM process, the thin passive film can be strongly attached to the surface. The anodic reaction for metal dissolution was hindered by the compact passive film, and exclusive oxygen evolution occurred on the surface of 304 stainless steel at low current density [33-34]:

$$2H_2O \rightarrow O_2 \uparrow + 4H^+ + 4e^- \tag{6}$$

Due to the protection of the compact passive film formed at low current density, the surface of lug boss can be well preserved during CRECM of 304 stainless steel. As a result, the surface is smooth without any corrosion, as shown in Figs. 7(a) and 8(a). In contrast, according to Fig. 14, the current efficiency for Inconel 718 persists high even at low current density. This is because the passive film formed on Inconel 718 in $NaNO_3$ solution is porpus and defective, and can hardly protect the inner material from corrosion [19]. As the current efficiency is less than 100%, it can be decuced that the predominant metal dissolution and slight oxygen evolution proceed in parallel on the surface of Inconel 718:

$$Me \rightarrow Me^{n+} + ne^- \tag{7}$$

$$2H_2O \rightarrow O_2 \uparrow + 4H^+ + 4e^- \tag{8}$$

As shown in Fig. 2(a), the predominant metal dissolution for Inconel 718 at low current density leads to substantial pitting corrosion even at a low current density of 1 A/cm^2. The surface of the lug boss on Inconel 718 is seiously corroded during CRECM, and the machining accuracy is reduced accordingly.

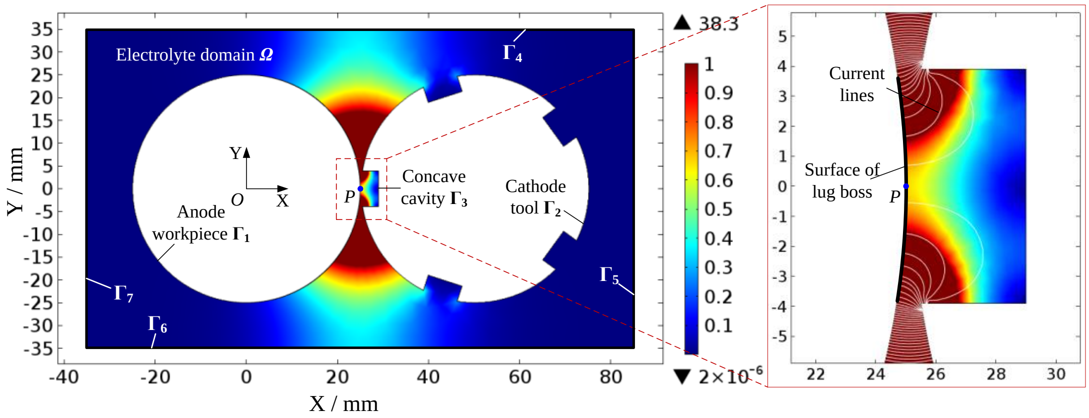

Figure 12. Current density distribution at a rotation angle of 0°.

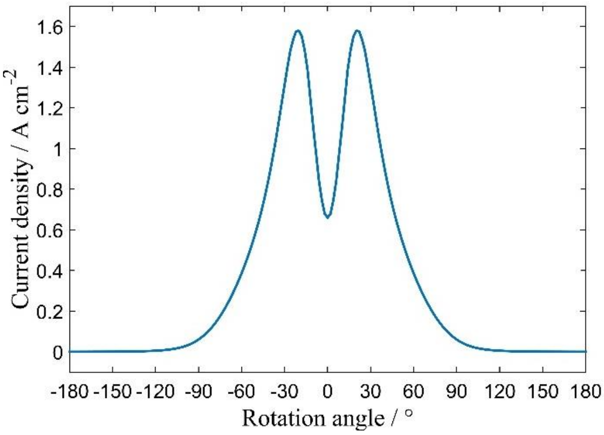

Figure 13. Current density at the midpoint *P* on the surface of lug boss at different rotation angles.

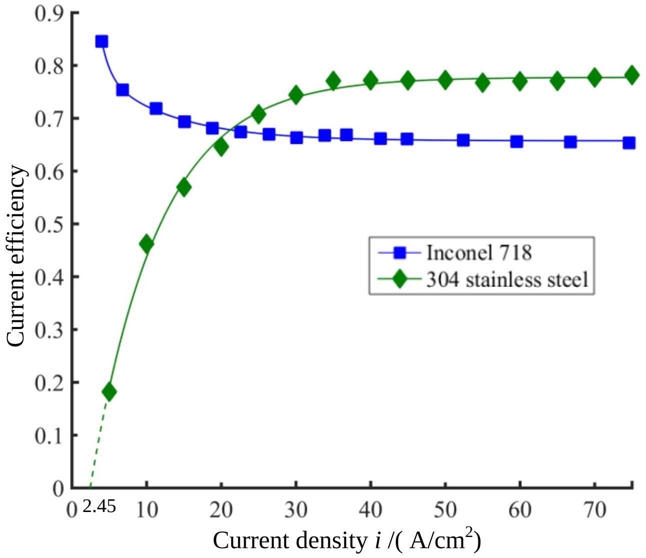

Figure 14. Current efficiency vs current density curves for 304 stainless steel and Inconel 718 in $NaNO_3$ solution.

3.2. *Improvement of machining performance*

On the outer surface of Inconel 718 engine casing parts, high lug bosses are commonly designed. The studies above indicate that Inconel 718 is vulnerable to corrosion even at low current densities (< 1A/cm^2), which will result in a serious corrosion and poor CRECM accuracy of high lug bosses. In contrast, 304 stainless steel exhibits superior machining performance during CRECM of lug bosses because of its favorable localization effect. Thus, a 304 stainless steel coating layer was used to improve the machining accuracy of a tall lug boss on Inconel 718. As shown in Fig. 15, the surface of the cylindrical Inconel 718 workpiece was covered with a thin 304 stainless steel coating layer using spraying technology. Since the 304 stainless steel coating will not be dissolved at low current densities during CRECM, it can be preserved on the surface of lug boss and thereby protects the inner Inconel 718 material from corrosion.

Lug bosses were fabricated on Inconel 718 via CRECM, as shown in Fig. 16. Fig. 16(a) shows a high structure (8.17 mm in height) with no coating layer. The surface of the lug boss is seriously corroded and large fillets are observed on the top. When a 304 stainless steel coating layer is used, the machining profile of the lug boss improves remarkably (Fig. 16(b)). The surface of the lug boss is much flatter when provided the protection of the 304 stainless steel coating layer than without it and trenchant edges can be seen in the top view. The contour lines of the lug boss cross-sections are compared in Fig. 17. The amount of corrosion on the surface is reduced from 0.81 mm to 0 mm.

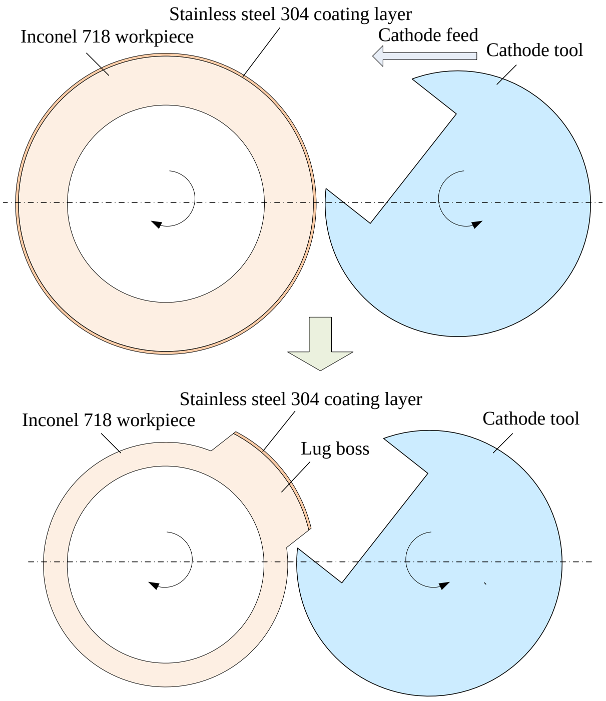

Figure 15. Principle of the use of a stainless steel 304 coating layer.

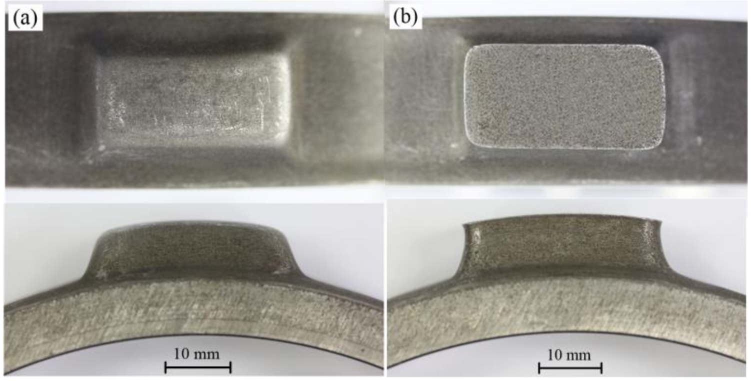

Figure 16. Lug bosses fabricated on Inconel 718 workpieces. (a) No coating layer; (b) With a stainless steel 304 coating layer.

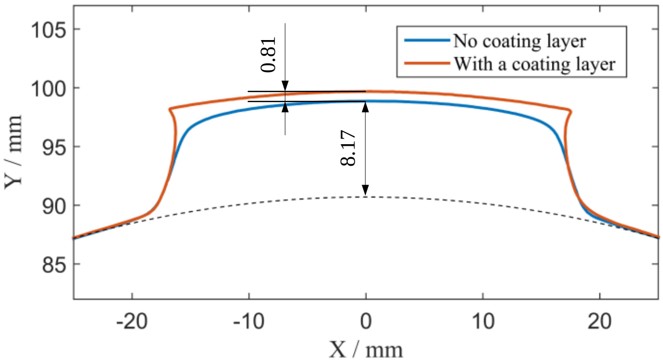

Figure 17. Lug boss cross-section contour lines.

4. CONCLUSIONS

The CRECM performances of 304 stainless steel and Inconel 718 alloy were investigated. The microstructures of surfaces corroded at different current densities were examined using SEM, EDX, and EIS. The profiles and surface qualities of the lug bosses machined on 304 stainless steel and Inconel 718 via CRECM were compared. The conclusions can be summarized as follows:

(1) SEM images and EIS results indicate that the surface of 304 stainless steel was smooth with no corrosion at a low current density of 1 A/cm^2 due to formation of a compact passive film. However, serious pitting corrosion occurred on the surface of Inconel 718 at 1A/cm^2 because of the defective passive film.

(2) Straight lug bosses with small fillet radii were fabricated on 304 stainless steel due to its favorable localization effect of anodic dissolution. In contrast, the sidewall of a lug boss on Inconel 718 was tapered and exhibited a large fillet radius because of serious corrosion on the top of the structure.

(3) A 304 stainless steel coating layer was used to improve machining accuracy of a high lug boss on Inconel 718 during CRECM. The experimental results show that the 304 stainless steel coating layer can protect the surface of the lug boss and improves machining accuracy remarkably.

ACKNOWLEDGEMENTS
This research was funded by National Natural Science Foundation of China (51805259), Natural Science Foundation of Jiangsu Province (BK20180431), China Postdoctoral Science Foundation (2018M642246), Jiangsu Key Laboratory of Precision and Micro-Manufacturing Technology and Young Elite Scientists Sponsorship Program by CAST.

References

1. K.P. Rajurkar, D. Zhu, J.A. McGeough, J. Kozak and A. DeSilva, *CIRP Ann. Manuf. Technol.*, 48 (1999) 567.
2. R.R. Venkata and V.D. Kalyankar, *Int. J. Adv. Manuf. Technol.*, 73 (2014) 1159.
3. K.P. Rajurkar, M.M. Sundaram and A.P. Malshe, *Proc. CIRP*, 6 (2013) 13.
4. F. Klocke, M. Zeis, A. Klink and D. Veselovac, *Proc. CIRP*, 6 (2013) 368.
5. Z.Y. Xu, Q. Xu, D. Zhu and T. Gong, *CIRP Ann. Manuf. Technol*., 62 (2013) 187.
6. D. Zhu D, Z.Z. Gu, T.Y. Xue and Zhu D, *Proc. CIRP*, 42 (2016) 121.
7. K.W. Mao and J.P. Hoare, *Corros. Sci*., 13 (1973) 799.
8. K.W. Mao, *J. Electrochem. Soc*., 118 (1971) 1876.
9. T. Haisch, E. Mittemeijer and J.W. Schultze, *Electrochim. Acta*, 47 (2001) 235.
10. C. Rosenkranz, M.M. Lohrengel and J.W. Schultze, *Electrochim. Acta*, 50 (2005) 2009.
11. M.M. Lohrengel, I. Klüppel, C. Rosenkranz, H. Bettermann and J.W. Schultze, *Electrochim. Acta*, 48 (2003) 3203.
12. M.M. Lohrengel and C. Rosenkranz, *Corros. Sci.*, 47 (2005) 785.
13. M. Schneider, N. Schubert, S. Höhn and A. Michaelis, *Electrochim. Acta*, 106 (2013) 279.
14. M. Weinmann, M. Stolpe, O. Weber, R. Busch and H. Natter, *J. Solid State Electr*., 19 (2015) 485.
15. Y.F. He, J.S. Zhao, H.X. Xiao, W.Z. Lu and W.M. Gan, *Int. J. Electrochem. Sci*., 13 (2018) 5736.
16. D.Y. Wang, Z.W. Zhu, H.R. Wang and D. Zhu, *Chin. J. Aeronaut*., 29 (2016) 534.
17. D.Y. Wang, Z.W. Zhu, B. He, D. Zhu and Z.D. Fang, *J. Manuf. Processes*, 35 (2018) 614.
18. Z.W. Zhu, D.Y. Wang, J. Bao, N.F. Wang and D. Zhu, *Int. J. Manuf. Technol*., 80 (2015) 1957.
19. D.Y. Wang, Z.W. Zhu, N.F. Wang, D. Zhu and H.R. Wang, *Electrochim. Acta*, 156 (2015) 301.

20. W. Ye, Y. Li, F.H. Wang, *Electrochim. Acta*, 51 (2006) 4426.
21. J.L. Lv and H.Y. Li. *Appl. Surf. Sci.*, 263 (2012) 29.
22. C.P. Gao, N.S. Qu, B. Ding and Y.Z. Shen, *Electrochim. Acta*, 295 (2019) 67.
23. N.P. Dai, L.C. Zhang, J.X. Zhang, Q.M. Chen and M.L. Wu, *Corros. Sci.*, 102 (2016) 484.
24. D. Zhu, N.S. Qu, H.S. Li, Y.B. Zeng, D.L. Li and S.Q. Qian, CIRP Ann. *Manuf. Technol*., 58 (2009) 177.
25. D.Y. Wang, Z.W. Zhu, J. Bao, and D. Zhu, *Int. J. Manuf. Technol*., 76 (2015) 1365.
26. X.F. Zhang, N.S. Qu and X.L. Chen, *Surf. Coat. Tech.*, 302 (2016) 438.
27. A.K.M. De Silva, H.S.J. Altena, and J.A. McGeough, *CIRP Ann*., 52 (2003) 165.
28. P.S. Pa, Electrochim. Acta, 54 (2009) 6022.
29. X.L. Fang, N.S. Qu, Y.D. Zhang, Z.Y. Xu, and D. Zhu, *J. Mater. Process. Technol*., 214 (2014) 36.
30. X.L. Chen, B.Y. Dong, C.Y. Zhang, H.P. Luo, J.W. Liu, Y.J. Zhang, and Z.N. Guo, *J. Mater. Process. Technol.*, 265 (2019) 138.
31. E. De vito, and P. Marcus, *Surf. Interf. Anal*., 19 (1992) 403.
32. M. Datta, H.J. Mathieu, and D. Landolt, *J. Electrochem. Soc*., 131 (1984) 2484.
33. D.Y. Wang, Bin He, Z.W. Zhu, Y.C. Ge, and D. Zhu, *J. Electrochem. Soc*., 165 (2018) 282.
34. M.M. Lohrengel, K.P. Rataj, and T. Munninghoff, *Electrochim. Acta*, 201 (2016) 348.